Modelling the Low-Pressure N_2–O_2 Plasma Afterglow to Determine the Kinetic Mechanisms Controlling the UV Emission Intensity and Its Spatial Distribution for Achieving an Efficient Sterilization Process

Kinga Kutasi,* Bachir Saoudi, Carlos D. Pintassilgo, Jorge Loureiro, Michel Moisan

The flowing afterglow of a N_2–O_2 microwave discharge intended to provide intense and spatially uniform UV emission for an efficient inactivation of bacterial spores is modelled with a 3-D hydrodynamic model leading to the spatial density distribution of the species in the reactor. The agreement of the calculated densities of the NO(A) and NO(B) UV emitting species with the corresponding measured emission intensities strongly supports the choice of the kinetic reactions retained in the model. In that respect, the specific contribution of N and O atoms to the spatial distribution of the NO(A) density (generating the NO_γ system) in the late afterglow is, for the first time, brought into relief.

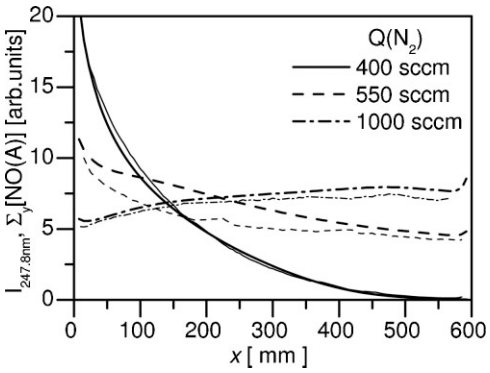

1 Introduction

1.1 Plasma Sterilization: Context

In the last decades, the use of polymer-based heat-sensitive tools in the medical praxis has increased the need for efficient and safe low-temperature sterilization methods that would not only ensure complete inactivation of microorganisms (e.g. vegetative bacteria, spores, viruses), but also possibly remove all infectious residues (e.g. pyrogens (endotoxins), prion proteins) on used instruments. To date, the most common low-temperature sterilization methods are either based on chemical treatments, which call for toxic active agents (e.g. ethylene oxide) and generate harmful effluents, or on exposure to γ radiation, which can alter the bulk properties of the polymers being sterilized.

The use of low-temperature plasmas appears as a promising solution to these drawbacks.[1,2] Low-temperature plasmas can be created either at atmospheric pressure or low pressures ($p \leq 10$ Torr). In fact, numerous experimental studies have been carried out over both pressure ranges using different discharge configurations: namely at atmospheric pressure,[3–17] in the mTorr[18–23] and Torr ranges,[24–31] employing various gas mixtures,

K. Kutasi, C. D. Pintassilgo, J. Loureiro
Instituto de Plasmas e Fusão Nuclear, Instituto Superior Técnico, 1049-001 Lisboa, Portugal
E-mail: kutasi@sunserv.kfki.hu
B. Saoudi, M. Moisan
Groupe de Physique des Plasmas, Université de Montréal, CP 6128, Succursale Centre-Ville, Montréal H3C 3J7, Québec, Canada
C. D. Pintassilgo
Departamento de Engenharia Física, Faculdade de Engenharia da Universidade do Porto, 4200-465 Porto, Portugal
K. Kutasi
Present address: Research Institute for Solid State Physics and Optics, Hungarian Academy of Sciences, POB 49, H-1525 Budapest, Hungary

Plasma Process. Polym. **2008**, *5*, 840–852

DOI: 10.1002/ppap.200800085

e.g. N_2,[18,20,23] O_2,[15,18,20,23] N_2–O_2,[9,18,23,29,32] Ar,[8,13,16] Ar–O_2,[26] Ar–H_2,[21] O_2–H_2O,[22] O_2–CF_4,[19] aiming at testing the sterilizing efficiency of these plasmas. Two generic plasma configurations are nowadays being investigated; sterilization takes place within the discharge region,[3,10,13,18–21] or in its flowing afterglow.[9,24,26,33] The flowing afterglow is particularly well adapted to provide a low gas temperature, practically free of charged species (avoiding ion bombardment damage to the exposed materials) with at the same time, depending on operating conditions, high concentrations of chemically active radicals (e.g. O and N atoms in the appropriate mixture), excited atomic and molecular species (e.g. metastable-state atoms and molecules), and/or high UV intensity radiation, all of these having some potential for the inactivation of microorganisms.

2 Summary of the Work Previously Done on the N_2–O_2 Flowing-Afterglow Directed at Spore Inactivation

2.1 Identification of the Species Participating in the Inactivation Process Taking Place in the N_2–O_2 Flowing Afterglow

The N_2–O_2 low-pressure (0.5–10 Torr) discharge flowing afterglow is known to yield long lifetime O and N atoms at high concentration levels. These chemically reactive species, by themselves, can inactivate microorganisms. But there is more to it; owing to the formation of NO excited molecules through N and O collisions in this afterglow (sometimes calling for a third body), intense UV photon radiation can be made available, such photons being a further possible efficient biocide agent. The UV photons are mainly emitted by radiative transitions of the NO($B^2\Pi$) and NO($A^2\Sigma^+$) excited states to the NO($X^2\Pi$) ground state; these generate the so-called NO_β and NO_γ systems, respectively[1]. Spore inactivation can thus result either from reactive atoms that cause erosion (etching) of the microorganisms or from UV photons that essentially damage the bacterium DNA material. A combination of these inactivation agents is also possible.

[1] According to Pearse and Gaydon,[34] the full NO_β system actually starts at 201.81 nm and extends up to 527.01 nm while the NO_γ system goes from 195.61 nm up to 345.8 nm. Nonetheless, under our experimental conditions (e.g. Boudam et al.[31]), these systems are observed to be restricted approximately to the 260–400 and 205–290 nm spectral ranges, respectively. Positive wavelength identification of these two system respective bandheads is confirmed when 3% O_2 or more is added to N_2: the NO_β system then disappears leaving the NO_γ system alone (Moisan et al. to be submitted). Gross et al.[56] reported a similar observation with a nitric oxide afterglow, the spectra range below 260 nm showing no NO_β contribution.

The first results using the N_2–O_2 flowing afterglow for sterilization purposes, disclosed in a patent in 1999, were reported by Moreau et al.[24]. It was shown that total inactivation of an initial 10^6 spore population can be obtained in such a flowing afterglow provided by a microwave discharge in a N_2–2% O_2 mixture at a 2 Torr gas pressure. This percentage of O_2 added to N_2 resulted from setting for maximum UV intensity (by tracking a given bandhead of the NO_β system) to achieve the fastest inactivation rate. The papers by the Montréal team that followed, provided valuable experimental data, such as, reliable survival curves, based on optimized microbiological protocols and controlled afterglow exposure conditions in the sterilization chamber. These results led to a better understanding of the microorganism inactivation mechanisms by the N_2–O_2 afterglow. In particular, the initial orientation of this team, namely the possibility of basing microorganism inactivation on UV photons rather than chemically active species, was well confirmed and documented. More recently, a detailed investigation of the UV spectrum correlated with the inactivation rate coefficient (made by the Montréal team but not reported yet) has shown that it is the NO_γ system, and not the NO_β system as stated in earlier publications, that is the main UV photon contributor. This confusion resulted from the fact that the relative intensity variation of any bandhead of these two systems as a function of the added O_2 percentage is similar in the 0–3% range, and in particular that the maximum UV intensity of both systems occurs at (almost) the same O_2 percentage. However, relying on published spore inactivation rates (''action spectra''[35,36]) and using high-pass (in terms of wavelength) optical filters, we have shown that the *Bacillus atrophaeus* spore inactivation rate is practically negligible at wavelengths $\geq$ 280 nm, implying that the NO_γ system, and not the NO_β system, is the one essentially providing the biocide photons (Moisan et al. to be submitted).

In the meanwhile, Villeger et al.[37] from Toulouse followed a different inactivation approach. Instead of aiming at maximizing the NO emission intensity through the added O_2 percentage, they rather relied on the action of N atoms synergistically with heat (temperature rise of the substrate is induced by N atoms recombination). Indeed, they showed that spore inactivation can be achieved also at 1–2 Torr in a pure N_2 flowing afterglow.[38] They also reported efficient sterilization conditions when adding O_2 to N_2 at the 5% level or more to obtain a high O-atom density but with still significant UV intensity.[29]

The sterilization process is required to have the same efficiency everywhere in the afterglow chamber, implying uniform spatial distributions of N and O atom densities to achieve the same with excited NO molecules. Modelling the density distributions of these species in the reactor should also bring more insight into the kinetics of the

microorganism inactivation process, eventually allowing for optimization of the system and providing indications for its scale-up.

2.2 Experimental Data on the Afterglow Species Densities

The densities of N and O atoms have been determined under various discharge conditions (gas pressure, flow rate and gas mixture composition). The absolute values of N and O atom densities have been measured by NO titration under dominant late afterglow conditions, at a fixed position, namely the reactor entrance.[26,27,29,31,39,40] N-atom density can be determined at several positions in the reactor, but this time only as a relative value, using, for instance, Bockel's method[41], which is based on the intensity measurements at 580 nm of the first positive system [$N_2(B,v'=11)$]. In earlier papers, measurements of the UV emission intensity in the late afterglow as a function of the added O_2% have been limited to the NO_β system (260–400 nm), in fact to a given band-head,[26,27,29,31,40] excluding the NO_γ system. However, for the reasons mentioned in the previous section, we need to know the contribution of the NO_γ system (205–290 nm). Therefore, both the NO(A) and NO(B) measured densities are reported below and considered for comparison purposes both on experimental ground and with the model.

In the afterglow chamber, besides the active species mentioned in the previous section and that are expected to lead to non-damaging sterilization, there are sometimes also (depending on operating conditions) metastable-state atoms and molecules as well as charged species, which can cause damage to the treated devices. For instance, our research team reported earlier a significant erosion of the spores and polymer materials when these are located in the vicinity of the discharge tube axis within the afterglow chamber.[42] This strong on-axis erosion is claimed[31] to result from the action of the $N_2(A)$, $N_2(a')$ metastable-state molecules, as well as of the N_2^+, N_4^+ nitrogen molecular ions, these various species being characteristic of the early afterglow. Boudam et al.[31] have shown that by increasing the distance from the plasma source to the afterglow chamber entrance and the percentage of added O_2, one could avoid, or at least limit, these damaging contributions from the early afterglow entering the sterilization chamber.

2.3 Summary of the Modelling Work Previously Achieved

The N_2–O_2 microwave discharge and the early afterglow that occurs immediately downstream from the discharge in the same discharge tube have been investigated initially by Pintassilgo et al.[43] by means of a 1-D kinetic model. The results of their model give insight into the time evolution of the species densities in the early afterglow, which translates into the travelling distance of these species between the plasma source and the chamber entrance, hereafter designated as the connecting zone. This information tells us how to reduce the early afterglow contribution into the chamber by adjusting the 'length' of the connecting zone. The 3-D hydrodynamic model developed afterwards by Kutasi et al.[44] as a complement to Pintassilgo et al.[43] kinetic model included the reactor chamber, which made possible the description of the whole sterilization system. The distribution of the gas temperature, together with the NO(B) and $O(^3P)$ relative densities, was on that occasion studied in the reactor for two different pressure values as functions of the gas flow rate, allowing to determine the conditions providing a low gas temperature in the reactor. This hydrodynamic model was then further improved by extending the list of species considered in the reactor and also by including surface recombination processes of the atomic species.[45] The calculated NO(B) relative densities predicted reasonably well the behaviour of the NO_β system emission intensity as a function of pressure and mixture composition, although with a significant shifting towards larger values of the (optimum) percentage of O_2 yielding maximum NO_β emission intensity.[46] At any rate, the model failed to reproduce correctly the emission of the NO_γ system stemming from the NO(A) excited molecules. This issue is solved in the current model by introducing new reaction pathways for the formation of the NO(A) state in the late afterglow. By the same token, the calculated percentage of added O_2 leading to maximum UV intensity, in contrast to previous models, is found close to the experimental one (not reported here) and, as will be presented, most observed features of the NO_γ emission are recovered.

3 Experimental Arrangement and Operating Conditions Considered in the Modelling

3.1 Experimental Arrangement

The N_2–O_2 flowing afterglow system to be modelled is the one developed at Université de Montréal for sterilization purposes. It is shown in Figure 1a with details on the discharge (and connecting) tube given in Figure 1b.

The discharge tube's inner diameter is 6 mm and it extends away from the surfatron launching gap on a distance x_1 before turning into a tube of 26 mm inner diameter and 120 mm length connecting to the reactor entrance plane; the widening of the tube occurs over approximately 20 mm. The distance x_1 is set here at 30 mm (for details on the influence of x_1, Boudam et al.[31]). The afterglow chamber (sterilizer), made from aluminium, has

DOI: 10.1002/ppap.200800085

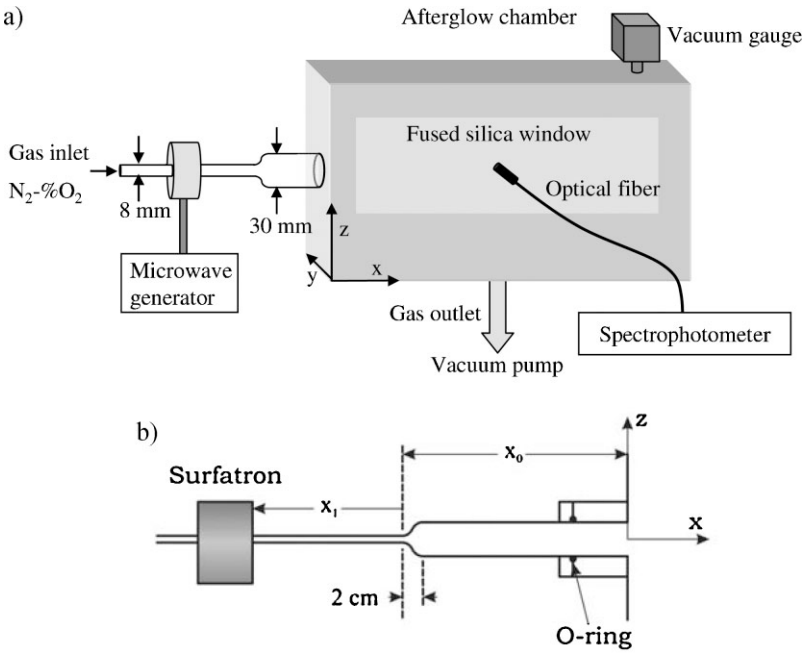

Figure 1. (a) Schematic representation of the basic flowing afterglow system as used for plasma sterilization purposes. It is comprised of the microwave-sustained plasma source (surfatron type[54]), operated at 2 450 MHz, and of a 50 L afterglow chamber (sterilizer). The discharge tube of 6/8 mm id/od connects to a larger 26/30 mm id/od tube; (b) configuration of the tube linking the discharge region to the afterglow chamber where x_o and x_1 are set at 120 and 30 mm, respectively; the tube axis, defining the chamber axis, is set at $z = 140$ mm (adapted from Boudam et al.[31]).

a parallelepipedic shape with internal dimensions of $60 \times 30 \times 28$ cm^3 yielding a 50 L volume. It is equipped with fused silica windows to allow for spectroscopic observations. The gas inlet and vacuum pumping outlet (located at the geometrical center of the bottom plate) are shown in Figure 1a. The power of the microwave sustaining field at 2 450 MHz is generally set at 100 W (2 W/L).

The discharge and afterglow light-emission intensities between 200–400 nm are integrated along the *y*-axis with a collimator (3 mm diameter and 50 mm length) that collects light along a 300 mm depth [chamber width (*y*-axis)], thus yielding moderate *x* and *z* spatial resolution. The recorded emission intensity is sent, to be analysed, through an optical fibre to a spectrophotometer, as indicated in Figure 1a; spectral resolution is generally 0.2 nm. The UV light emission intensity in the reactor is plotted along the *x*- and *z*-axes (see Figure 1a) at wavelength 247.8 nm, corresponding to the bandhead generated by the transition from the NO ($A^2\Sigma^+$, $v = 0$) excited state to the NO ($X^2\Pi$, $v = 2$) ground state (NO_γ system), and at 304.3 nm, corresponding to the bandhead generated by the transition from the NO ($B^2\Pi$, $v = 0$) excited state to the NO ($X^2\Pi$, $v = 7$) ground state (NO_β system); these levels are shown on the potential curve in Figure 5 further down.

3.2 Important Modelling Parameters and Range of Operating Conditions Considered in the Modelling

The modelling needs to take into account the following elements: (i) the distance between the plasma source and the entrance of the post-discharge reactor ($x_1 + x_0$), as well as the geometry of the discharge tube connecting them; (ii) fixed discharge parameters such as tube inner radius, microwave field frequency, input power; (iii) variable parameters such as gas mixture composition, gas pressure and gas flow rate. The position of the gas inlet and pumping outlet, which act on the hydrodynamics of the gas flow, also influences the density distribution of the species, given the structure and dimensions of the chamber.

Comparison between experiment and theory is made for the following ranges of conditions: (i) N_2–χO_2 mixtures, where χ designates the percentage of O_2 added to N_2, the carrier gas, actually varied between 0.2 and 2%; (ii) gas pressures in the 0.6–10 Torr range; (iii) gas flow rates between 400 and 1 000 sccm; (iv) discharge tube inner radius is 3 mm (details on tube geometry and distance to chamber entrance under Section 3.1 experimental arrangement); (v) applied field frequency 2 450 MHz. Nonetheless, at the time of calculations, more extended conditions were examined considering additionally tube inner radii of 6 and 10 mm.

Section 4 that follows, describes the basic elements of the model, while Section 5 displays the modelling results and compares them with experimental data and Section 6 is the conclusion.

4 Model

The model developed aims at recovering the various species present in the flowing afterglow chamber and their densities as functions of position within it. Some of these species can come from the early afterglow only (i.e. are not created further in the late afterglow); in such a case, these species are generally localized around and along the afterglow-chamber axis. On practical ground, as a rule to minimize damage, we try to reduce the early afterglow

contribution and operate in a dominant late afterglow mode everywhere in the chamber.

The applied model is described in detail in ref.[44]. Briefly, the species densities in the discharge are calculated with the 1-D self-consistent model of the flowing N_2–O_2 microwave discharge based on solutions to the electron Boltzmann equation coupled to a system of rate-balance equations for the neutral and charged heavy-species.[43] The time evolution of the species densities in the early afterglow, which occurs downstream from the discharge in the connecting tube, is determined by solving the same system of rate-balance equations as in the discharge, this time in the absence of excitation by electron impact.[43] The time-dependent solutions obtained in this way constitute the initial conditions for the 3-D hydrodynamic model that provides the evolution of the species densities in the reactor. The hydrodynamic model is comprised of (i) the total mass conservation equation, (ii) the total momentum conservation equation, (iii) the total energy (temperature) conservation equation and (iv) the continuity equations for the plasma components.[44] The velocity distribution of the fluid in the connecting zone is also determined with the 3-D hydrodynamic model.

The species taken into account in the modelling and the set of gas-phase reactions describing the kinetics of species that are considered in the discharge tube and in the post-discharge chamber are listed in ref.[43,44,47]. A detailed description of the kinetics of N_2 electronic-state excitation can be found in Shakhatov and Lebedev.[48] In fact in each of the three zones, the same set of reactions is taken into account; however, in the 3-D model of the post-discharge chamber, we omit those processes involving species that can be neglected: the $N_2(X^1\Sigma_g^+,\ v>0)$ and $O_2(X^3\Sigma_g^-, v' > 0)$ vibrational distributions; the electronic states of molecular and atomic nitrogen, namely $N_2(B'^3\Sigma_u^-, C^3\Pi_u, a'^1\Sigma_u^-, a^1\Pi_g, w^1\Delta_u)$ and $N(^2D,\ ^2P)$; the NO_2(A) state; the main positive ions $N_2^+(X^2\Sigma_g^+)$, $B^2\Sigma_u^+$, N_4^+, O_2^+, O^+ and NO^+ are not implied in reactions involving neutrals and negative ions O^-. The importance of the processes taking place in the discharge, in the early afterglow and in the late afterglow, is discussed in ref. [43,49] and ref.[44,47] respectively.

It is well known that recombination of atoms on a surface can be very effective.[45] In the present case, in contrast to the previously cited papers, all possible surface losses of N and O atoms, which include those on the Pyrex discharge-tube wall, on the silica windows and the aluminium walls of the reactor were taken into account. The surface loss probabilities of the N and O atoms on aluminium are taken as 1×10^{-3} and 1.7×10^{-3}, respectively,[50] while on silica and Pyrex surfaces these are 1×10^{-4} for both atomic species.[51] The N and O atoms are assumed to recombine into N_2 and O_2, respectively. As shown in ref.,[45] even when assuming that these atoms all recombine onto surfaces as NO molecules, their contribution to the UV emission in the chamber is found negligible. More details about the effect of surface losses in a large post-discharge reactor can be found in ref.[45,52].

5 Results and Discussion

5.1 Effect of the Discharge Tube Radius on N and O Atom Densities

The density of the radiative species NO(A) and NO(B) depends on the N and O atom densities (see further Section 5.3) and, in turn, the density of N atoms is influenced by the radius of the discharge tube as we discuss.

Recall that the loss of charged particles in the discharge, within the pressure range considered, is due to their diffusion to the tube wall on which they recombine. The smaller the tube diameter, the faster the particles reach the tube wall resulting in a higher surface loss, hence a higher electron 'temperature' to compensate for this increased loss.[53] At the same time, from the characteristics of surface-wave sustained discharges, we know that the smaller the tube radius, the higher the electron density as a result of the surface-wave attenuation properties along the discharge tube.[54] Therefore, the number of particles ionized or dissociated per unit volume is larger in smaller radius tubes; the electron energy is higher and the density of electrons is larger, hence a higher yield of N atoms since the dissociation of N_2 results from electron impact. In contrast, in a N_2–O_2 plasma, with a low O_2 content, the O atoms are essentially produced via the following heavy-particle reactions:

$$N_2(B^3\Pi_g) + O_2(X^3\Sigma_g^-) \rightarrow N_2(X^1\Sigma_g^+, v=0) + O + O \qquad (1)$$

and

$$N(^4S) + NO(X^2\Pi) \rightarrow N_2(X^1\Sigma_g^+, v \simeq 3) + O \qquad (2)$$

These processes are only indirectly influenced by the electron energy. Indeed, the dissociation by electron impact on $O_2(X^3\Sigma_g^-)$, $O_2(a^1\Delta_g)$ and $O_2(b^1\Sigma_g^+)$ provides minor contributions only, less than 10%, to the O-atom production, this mechanism being predominant at larger O_2 percentages only.

Figure 2 shows the densities (relative to the total gas density) of $N(^4S)$ and $O(^3P)$ atoms at the end of the discharge for three different values of the discharge tube radius at a gas pressure of 2 Torr in a N_2–1%O_2 mixture and at a 2 450 MHz microwave frequency. The highest calculated $N(^4S)$ density is found for the smallest tube radius, as already reported experimentally by Mérel

DOI: 10.1002/ppap.200800085

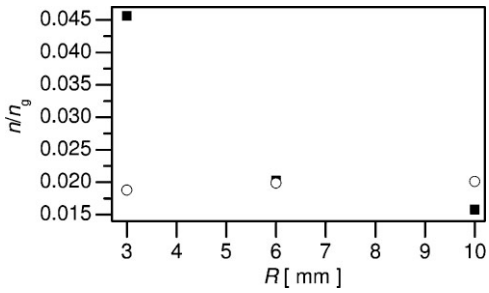

Figure 2. Calculated N(^{4}S) (■) and O(^{3}P) (○) densities (relative to total gas density) at the end of the surface-wave discharge as functions of the discharge tube radius at 2 Torr, N_2–1% O_2 and 2 450 MHz.

et al.[55]; while, under the present operating conditions, the O(^{3}P) density variation with radius is not significant in agreement with the fact that O(^{3}P) does not mainly arise from an electron impact process.

5.2 Species Time Evolution in the Early Afterglow: Determining the Length of the Connecting Zone that Ensures a Pure Late Afterglow

In contrast to the discharge region, the early- and late afterglows are characterized by the absence of a sustaining microwave electric field. The early afterglow comprises nonetheless a significant amount of atomic and molecular ions and a relatively high density of metastable-state atoms and molecules, both these types of species being negligible in the late afterglow. This early afterglow content decreases with time, either totally or by several orders of magnitude before reaching a plateau value. Making the connecting zone between the plasma source and the chamber entrance long enough allows us, as already mentioned, to minimize the concentration of early afterglow species in the chamber and thus to reduce damage (e.g. erosion) to materials during the sterilization process (more with Figure 3).

In this section, we examine the time evolution of the densities of the discharge species (ions and neutrals, metastable-state species) as they enter the early afterglow region and flow through it. The early afterglow starts with the depopulation of all these species (with delay for some charged species); then, after a while, some of these species reach a plateau value while others go on decreasing.

The length of this connecting region can be expressed in terms of the flight-time of species within it. The (common) flight-time of the species, for a given tube length, is estimated from the velocity field calculated with the 3-D hydrodynamic model in this connecting zone. The relative (to total gas density) densities of the species coming into the reactor are then determined from the time-dependent densities obtained with the 1-D kinetic model. In what

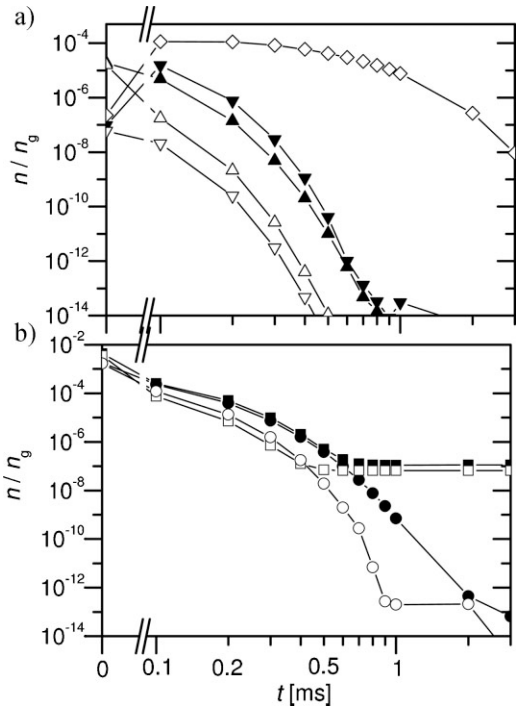

Figure 3. Time evolution in the early afterglow zone of the densities (relative to gas density) of different species under the 2 Torr condition, at two percentages of added O_2 to N_2 (a) for N_2^+: (▲) 0.2%, (△) 2%; N_4^+: (▼) 0.2%, (▽) 2% and NO^+: 0.2% (◇); (b) for N_2(A): (■) 0.2%, (□) 2%; N_2(a′): (●) 0.2%, (○) 2%.

follows, we investigate in detail the case where the gas pressure is 2 Torr with an added percentage χ of O_2 to N_2, successively 0.2 and 2%, at a 1 000 sccm gas flow rate. Figure 3a and b show the time evolution of the densities, in the early afterglow, of the ions and metastable molecules, respectively, which both are believed to play a major role in the damage to materials exposed to plasma sterilization.

Figure 3a shows that, with the exception of the NO^+ ion, the density of the N_2^+ and N_4^+ ions decreases by more than eight orders of magnitude within 1 ms, reaching density values that ensure that no damage can result from these species. As far as the NO^+ ion is concerned (at 2% O_2), its density slightly increases initially, goes through a quasi-plateau and then decreases slowly, ending at 2 ms with a value of two orders of magnitude lower than its initial one[2]. Previously, we have shown experimentally[31] that the N_2^+ and N_4^+ ions were not present in the sterilization chamber under our usual operating conditions (Section

[2] NO^+ is a long living ion, populated through charge exchange of N^+, O^+, N_2^+ and O_2^+ in collision with neutral species: NO, N, O, N_2, O_2. It is the dominating ion in a N_2–O_2 late afterglow.[49] It could contribute together with N_2(A) to the specific erosion damage observed on the discharge axis in the afterglow chamber.[31] The calculated NO^+ density does not vary significantly with the percentage of added O_2.

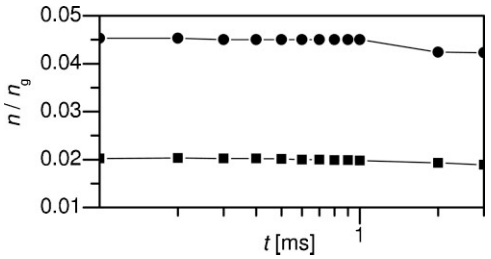

Figure 4. Time evolution in the early afterglow zone of the O(^{3}P) (■) and N(^{4}S) (●) densities (relatively to total gas density) at 2 Torr and with a N_2–1%O_2 mixture composition.

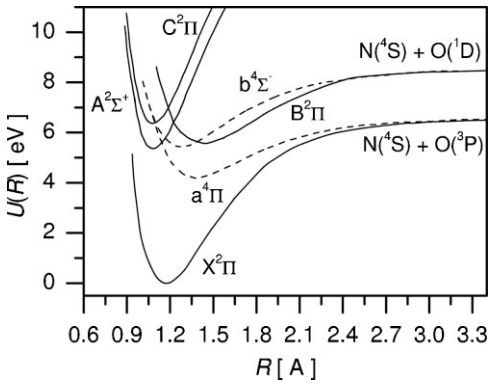

Figure 5. Potential energy curves of the NO states where *R* is the internuclear distance with indications as to the state of the O atom involved in the formation of the NO($b^4\Sigma^-$) and NO($a^4\Pi$) molecular states (adapted from[57]).

3.1). However, not knowing that NO^+ ions were formed, we did not look for them experimentally through emission spectroscopy.

Figure 3b shows the time evolution of the two main N_2 metastable-states. The N_2 (a′) molecule decreases by ten orders of magnitude within 2 ms whereas the N_2 (A) molecule, after an initial decrease by approximately four orders of magnitude over 0.5 ms, reaches a plateau that extends beyond at least 2 ms. The calculations show that varying the O_2% from 0.2 to 2 does not lead to an appreciable reduction in the N_2 (A) density.

Figure 4 shows the time evolution in the early afterglow in the densities of O(^{3}P) and N(^{4}S) atoms (relative to total gas density), these atoms contributing to the NO (A) and NO (B) molecules formation in the chamber. The density of O(^{3}P) does not vary during at least the first 3 ms, while the N(^{4}S) density decreases, but barely, after 1 ms. We further note that, at 1% O_2, there is approximately two times more N than O atoms. The fact that N and O atom densities keep constant in the whole transition zone is strongly supported by the experiments where an increase in the surfatron distance to the chamber entrance (varying x_1 from 30 mm to 100 mm) shows no significant changes in these densities (Figure 14 in Boudam et al. [31]).

Summarizing the results from Figure 3 and 4, we can conclude that adjusting the length x_1 such that the flight-time[3] of species in the connecting zone is at least 2 ms ensures that charged and metastable-state species are sufficiently reduced in density while, at the same time, the N and O atom densities are not much reduced, as required to achieve a significant UV emission intensity leading to efficient microorganism inactivation.

[3] At lower gas pressures for the same gas flow rate, higher velocities, hence significantly shorter flight times, are obtained in the transition zone. This explains why a more pronounced presence of the early afterglow (presence of ions and metastables) has been observed in the reactor when operating at 0.6 Torr compared to 2 Torr for a given x_1 value.[31]

5.3 UV Radiation

The main UV photon contribution in a N_2–O_2 discharge and its afterglows comes from the excited NO molecules in the $C^2\Pi$, $B^2\Pi$ and $A^2\Sigma^+$ states, listed here in decreasing order of energy, as can be seen in Figure 5. Transitions from these upper levels to the NO($X^2\Pi$) ground state yield the NO_δ, NO_β and NO_γ systems, respectively. The NO_δ system (182.8–198.5 nm as observed by us) is generally the one with the lowest emission intensity, while the intensities of the NO_γ (205–290 nm) and NO_β (260–400 nm) systems can be of the same order of magnitude.

5.3.1 UV Radiation in the Discharge and Early Afterglow

In the discharge, the emission intensity of the NO_γ system clearly dominates over that of the NO_β system, since here the NO(A) molecules are predominantly created by a two-body reaction of the highly populated $N_2(A^3\Sigma_u^+)$ state with the NO($X^2\Pi$) ground state, namely

$$N_2(A^3\Sigma_u^+) + NO(X^2\Pi) \rightarrow NO(A^2\Sigma^+) + N_2(X) \qquad (3)$$

while the NO(B) molecules are populated through a three-body (hence less probable) re-association of N and O atoms (Equation (4–6) in Section 5.3.2). Since this occurs in the discharge, the population density of the NO(A) state is constant in time because the density of both the N_2(A) and NO(X) states is constant.

In contrast, in the early afterglow, as shown in Figure 6, the calculated relative density of the NO(A) molecules decreases markedly as a function of the species flight-time *t* (from the end of the discharge, $t = 0$ ms, to the beginning of the late afterglow), actually by three orders of magnitude during the first 0.2 ms. Referring to reaction (1), this can be explained by the decrease in both the N_2(A) and NO(X) state densities with time in the early afterglow

DOI: 10.1002/ppap.200800085

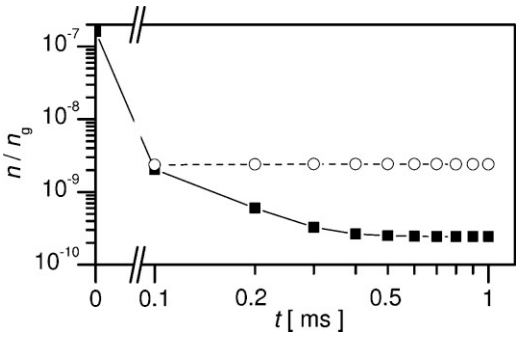

Figure 6. Calculated densities of NO(A) (■) and NO(B) (○) molecules (relatively to total gas density) as functions of the species flight-time t in the early afterglow region.

time period. According to Figure 6 and 3b, the NO(A) and N_2(A) densities decrease at approximately the same rate during this time period. At longer flight-times, namely from 0.6 to 2 ms, the N_2(A) state density is constant, but at a value three orders of magnitude lower than the initial one (Figure 3b), as a matter of fact yielding a much lower, but constant, NO(A) density (Figure 6).

Figure 6 shows that the density of the NO(B) state is constant throughout the early afterglow time period examined. Although, the density of the NO(A) molecules is higher at the beginning of the early afterglow time period, because it decreases strongly as the early afterglow elapses, the density of the NO(B) state ends up approximately an order of magnitude higher than that of the NO(A) state after 0.4 ms. These values, at given elapsed times in the early afterglow, are assumed to be the initial NO(A) and NO(B) densities at the entrance of the afterglow chamber.

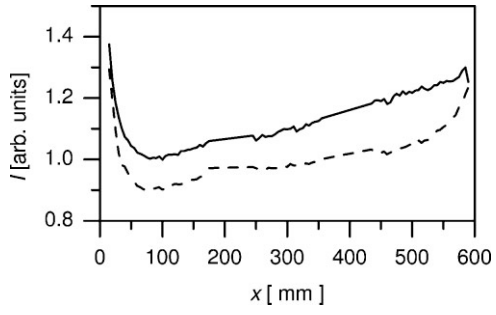

Figure 7. Observed emission intensity as a function of axial position along the afterglow chamber at $z = 140$ mm (afterglow axis) of bandheads of the NO_β system (304.3 nm: – – – –) and NO_γ system (247.8 nm: ——). The emission intensities displayed account for the spectral response of the spectrophotometer. The percentage of O_2 added to N_2 was set in each case to achieve maximum emission intensity. Corresponding gas flow rates: 700 sccm N_2 and 4 sccm O_2 for the NO_β emission, 800 sccm N_2 and 6 sccm O_2 for the NO_γ emission, N_2 gas pressure in both cases at 2 Torr.

5.3.2 UV Radiation in the Late afterglow

The NO($B^2\Pi$) state in the late afterglow is created through three successive reactions. At the start, there is a three-body re-association of N and O atoms implying mostly N_2 as the third body:

$$N(^4S) + O(^3P) + N_2 \rightleftarrows NO(a^4\Pi) + N_2 \quad (4)$$

It is followed by a collision-induced electronic transition from the NO($a^4\Pi$) to NO($b^4\Sigma^-$) state:

$$NO(a^4\Pi) + N_2 \rightarrow NO(b^4\Sigma^-) + N_2 \quad (5)$$

and then by a collision-induced transition from the NO($b^4\Sigma^-$) to NO($B^2\Pi$) state:

$$NO(b^4\Sigma^-) + N_2 \rightarrow NO(B^2\Pi) + N_2 \quad (6)$$

The $A^2\Sigma^+$ excited state of the late afterglow was assumed in previous publications to result only from equation (3) kinetic pathway. In such a case, the calculated NO(A) density, consequently the emission intensity of the NO_γ system, is found to be two-to-three orders of magnitude (depending on the mixture composition) lower than that of the NO_β system (see Figure 8 and 10 in Pintassilgo et al.[46]). In order to retrieve the experimentally observed behaviour of the NO_γ system, another creation pathway for NO(A) has been introduced in the present paper as suggested by Gross et al.[56], somehow similar to the three-body reaction (4) leading to the NO(B) state, namely

$$N(^4S) + O(^3P) + (N_2) \rightarrow NO(A^2\Sigma^+) + (N_2) \quad (7)$$

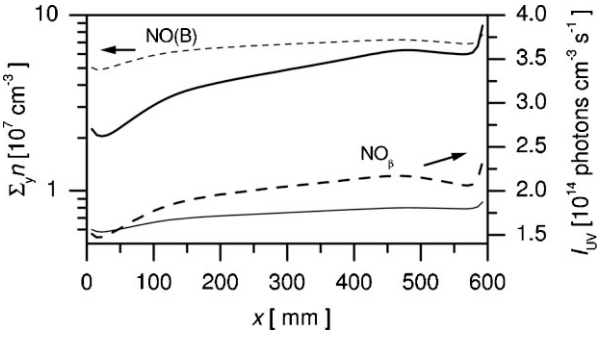

Figure 8. Calculated summed density along y of the NO(A) (——) and NO(B) (– – – –) levels (thin lines) and calculated corresponding UV emission intensity NO_γ and NO_β (thick lines) as functions of axial position in the chamber, x, at $z = 140$ mm (afterglow chamber axis), in both cases at 1000 sccm N_2 and 8 sscm O_2 gas flow rates under a 2 Torr gas pressure.

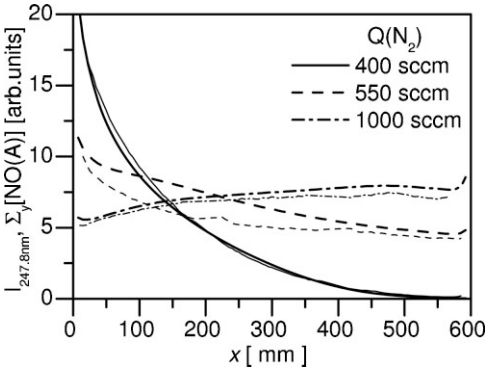

Figure 9. Measured (given thin line shape) emission intensity at 247.8 nm and (normalized) calculated (same line shape but thicker) density of NO(A) molecules as functions of position x at $z = 140$ mm (afterglow axis) in the reactor at 2 Torr, for three different N_2 gas flow rates Q with an O_2 flow rate set to 8 sccm.

where the brackets around N_2 indicate that it can be a two- or a three-body reaction. This kinetic pathway can be decomposed, according to Gross et al.[56], as follows:

$$N(^4S) + O(^3P) \rightleftarrows NO(a^4\Pi) \rightleftarrows NO(C^2\Pi, v = 0) \quad (8)$$

i.e. a collisional process involving N and O atoms, followed either by a collision-induced electronic transition implying mostly N_2:

$$NO(C^2\Pi) + N_2 \rightarrow NO(A^2\Sigma^+) + N_2 \quad (9)$$

hence the sequence of reactions 8 and 9 can be considered as a three-body reaction, or by cascade radiation:

$$NO(C^2\Pi) \rightarrow NO(A^2\Sigma^+) + h\nu \quad (10)$$

hence reactions 8 and 10 constitute a two-body reaction.

At any rate, under our working pressure range, the $A^2\Sigma^+$ state is populated in the end mainly from the $C^2\Pi$ state. Reaction 3 is included in the calculations for NO(A), but is found not to play a significant role.

The rates for the above-presented creation pathways (4–10) are taken from Gross et al.[56] In the case of the NO(B) state, a single three-body reaction is used: $3.09 \times 10^{-34}(T/300)^{-1.40}$ cm^6·s^{-1}, while in the case of NO(A) two reaction rates are given, one for a two-body reaction which involves the reactions 8 and 10: $1.18 \times 10^{-17}(T/300)^{-0.35}$ cm^3·s^{-1}, and one for a three-body reaction which involves the reactions 8 and 9 consecutively: $2.12 \times 10^{-34}(T/300)^{-1.24}$ cm^6·s^{-1}.

Figure 7 shows the observed emission intensity as a function of axial position along the afterglow chamber of bandheads of the NO_β system (304.3 nm) and NO_γ system (247.8 nm). The percentage of O_2 added to N_2 was set in each case to achieve maximum emission intensity for the given bandhead. Axial variation of the UV intensity is found to be similar for both emissions.

Figure 8 displays the calculated population densities, summed over the y-axis, of the NO(A) and NO(B) levels in the late afterglow and their corresponding calculated emission intensities as functions of the axial position x. Although the NO(A) density is lower than that of NO(B) by about one order of magnitude all along the reactor x-axis, the intensity of the UV radiation originating from the NO(A) level is higher, since its radiative frequency, 4.5×10^6 s^{-1}, is more than one order of magnitude higher than that of NO(B), 3×10^5 s^{-1}. The fact that the calculated intensity of the NO_γ emission is higher than that of the NO_β emission agrees with the experiment, as shown in Figure 7, except close to the entrance plane.

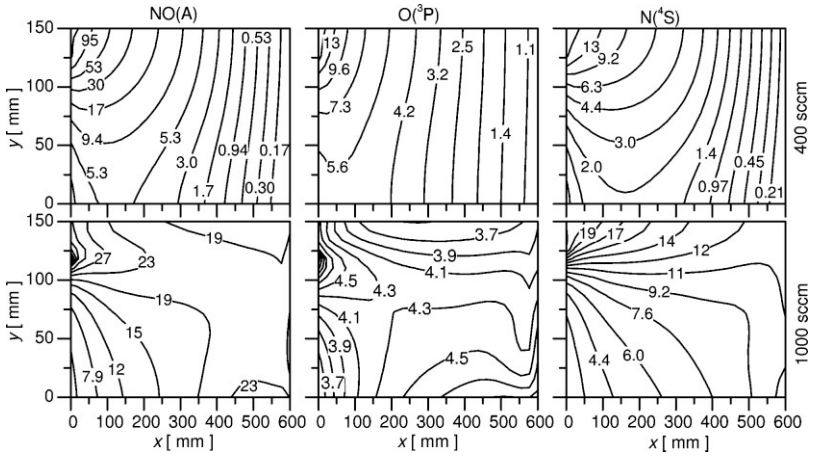

Figure 10. Calculated density distributions in the half x–y plane at the afterglow chamber axis ($z = 140$ mm) in the reactor at 2 Torr for: NO(A) (first column), O(^{3}P) (second column) and N(^{4}S) (third column) at 400 sccm (first row) and 1 000 sccm (second row) N_2 gas flow rate with an O_2 flow rate set to 8 sccm. The densities are given in 10^5 cm^{-3} units for NO(A) and in 10^{14} cm^{-3} units for O(^{3}P) and N(^{4}S).

5.4 Influence of the Gas Flow Rate

The validity of the model is assessed by comparing, under different gas flow rates, the measured intensities (spatially integrated along the y-axis) with the calculated densities (summed over the y-axis) of the upper level of the related emitting species, normalizing these densities (therefore expressed in arbitrary units) to fit the emission intensities at $x = 10$ mm (the same normalization factor, determined at 400 sccm, is used all over).

Figure 9 shows the measured UV intensity at 247.8 nm [band head of the transition between the NO($A^2\Sigma^+$, $v = 0$) state and the NO($X^2\Pi$, $v = 2$) state transition] and the (normalized and integrated over the y-axis) calculated NO(A) density

DOI: 10.1002/ppap.200800085

$[\sum_y[NO(A)]_{xyz}]$ as functions of the axial distance x at the afterglow chamber axis ($z = 140$ mm), for a total pressure of 2 Torr and at three different N_2 gas flow rates: 400, 550 and 1 000 sccm, for an O_2 gas flow rate set at 8 sccm. A good agreement is found between the calculated and measured data, especially at 400 and 1 000 sccm. The measured UV intensities and calculated emitting level densities being spatially integrated along the y-axis are thus functions of x and z. Figure 9 suggests that the (integrated along y and at a given z value) NO(A) density becomes more uniform in the x direction as the gas flow is increased; at the lowest flow rate plotted, the NO(A) density is maximum close to the plasma source while for flow rates above 800 sccm (curve not shown), this density starts to be larger near to the wall opposite to the gas inlet, as confirmed by the 1 000 sccm curve shown in the figure. Recovering such detailed experimental features from the calculations is an indication of the excellent predicting capabilities of the model.

The spatially resolved (x, y, z) calculated densities enable us to access interesting local features that are masked experimentally by the y-axis integration process (even on the x and z axes the spatial resolution is limited due to a non-parallel beam collimation). Figure 10 shows the calculated density distribution of NO(A), $O(^3P)$ and $N(^4S)$ states in the half x–y plane [from $y = 0$ (front-wall) to $y = 150$ mm (symmetry plane)] at $z = 140$ mm (discharge tube axis) for N_2 flow rates of 400 and 1 000 sccm. As already suggested by the experimental data (integrated emission intensity along y) at 400 sccm (Figure 9), the NO(A) density decreases significantly with x in the reactor, in fact by approximately three orders of magnitude from the entrance to the opposite wall. This appears related to the corresponding decrease with axial distance mostly of the N atom density. In the case of a 1 000 sccm gas flow, the detailed features provided by the spatially resolved density show that the non-uniformity present, nonetheless relatively small, is mainly located in the vicinity of the entrance chamber plane, most probably due to a relatively higher speed and more directed gas flow as compared to 400 and 550 sccm. Figure 10 shows that, at 1 000 sccm of N_2, the $O(^3P)$ density is quasi-uniform in the reactor, leading us to conclude that the predicted slight non-uniformity of NO(A) at that flow rate is induced by the N atom distribution since it is less uniform than that of the O atoms.

5.5 Effect of the Total Gas Pressure on Species Distribution in the Afterglow Chamber

Figure 11 shows the calculated NO(A) density integrated over the y axis ($\sum_y[NO(A)]_{xyz}$), as a function of axial position at two different total gas pressures for flow rates

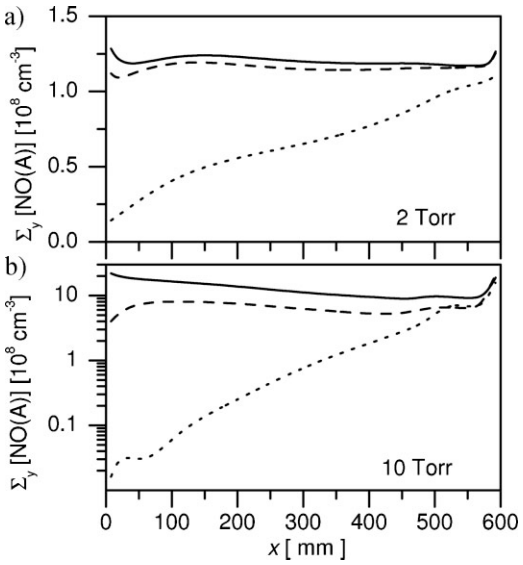

Figure 11. Calculated summed density over y of NO(A) state molecules as a function of x at three z positions: 140 mm (——), 105 mm (– – – –) and 35 mm (·····) in the reactor at (a) 2 Torr; (b) 10 Torr, in both cases with 1 000 sccm N_2 and 15 sccm O_2 gas flow rates (1.5% O_2).

of 1 000 sccm N_2 and 15 sccm O_2 at three different z positions in the reactor, including the afterglow axis $z = 140$ mm. These calculations have been performed with a 1 ms flight-time at the chamber entrance at each pressure considered, knowing that the results would be quite similar when considering instead a 2 ms flight-time (see Figure 3 and 4). The calculated NO(A) density at and close to the axis ($z = 140$ and 105 mm, respectively) is almost uniform as a function of x at both 2 and 10 Torr (Figure 11a and b). In contrast when moving sufficiently away from the axis ($z = 35$ mm, recall that the chamber bottom wall is at $z = 0$), the calculated value, at both pressures, increases markedly from the chamber entrance wall to the opposite wall; more specifically, it varies approximately by a factor of 5 at 2 Torr and by more than a factor of 100 at 10 Torr. These results are in accordance with the experimental observations at 2 Torr, at and close to the axis, when comparing with Figure 12a; far away from the axis ($z = 35$ mm), the NO(A) density is observed, as predicted by calculations, to increase also from the entrance wall towards the opposite wall, which it does at least up to two-third of the chamber length. At 10 Torr, at the three z heights considered, the variation trend of the NO(A) density starting from the chamber entrance is as predicted by theory; the difference between theory and experiment is however more pronounced at $z = 105$ mm; past the mid axis x position, both calculation and experimental results merge. As far as the absolute density of the NO(A) state is concerned, the calculations show (Figure 11) that its value is, as a rule, higher at the higher gas pressure.

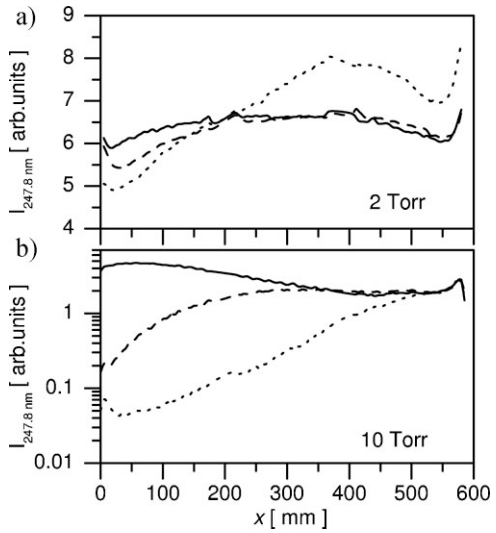

Figure 12. Measured emission intensity at 247.8 nm as a function of x recorded at three z positions: 140 mm (——), 105 mm (– – – –) and 35 mm (·····) in the reactor at: (a) 2 Torr; (b) 10 Torr, in both cases with 1 000 sccm N_2 and 15 sccm O_2 gas flow rates (1.5% O_2).

However, experiments show that the NO emission intensity at 2 Torr is almost always higher than that at 10 Torr throughout the reactor (Figure 12).

In what follows, we examine to what extent the NO(A) density depends on the N(^{4}S) and O(^{3}P) atom densities. Figure 13 provides spatially resolved density distribution of NO(A), N(^{4}S) and O(^{3}P) in the $x-z$ plane at three different gas pressures. It shows that uniformity of the NO(A) species in the whole reactor volume is obtained only at 2 Torr. At 5 and 10 Torr, the axial density distribution of the NO(A) state at the discharge (and flow) axis is again almost constant, but when departing from this axis it decreases sharply (as displayed in Figure 11). Figure 13 also shows that the O-atom density increases with gas pressure but remains spatially almost uniform throughout the reactor chamber with a slightly higher value around the axis. In contrast, the N-atom density, for a given pressure value, is the highest at the axis and it decreases transversally to it, this decrease becoming more important as the pressure is increased. It therefore comes out that the calculated spatial variations of the NO(A) density reflect the N-atom spatial density variations, and not those of O atoms. The conclusion drawn from the calculations as concerns the respective role of N and O atoms on the emission intensity stemming from the NO(A) level is similar to that inferred from the experimental data obtained for NO(B), see Figure 15 of Boudam et al.[31], i.e. the NO(B) emission intensity follows the behaviour of N atoms and not that of the O atoms.

In summary to this section, the model reproduces quite correctly the major observed trends as far as the spatial distribution of the NO(A) density at different pressures is concerned, but fails to predict the pressure dependence of its absolute density value.

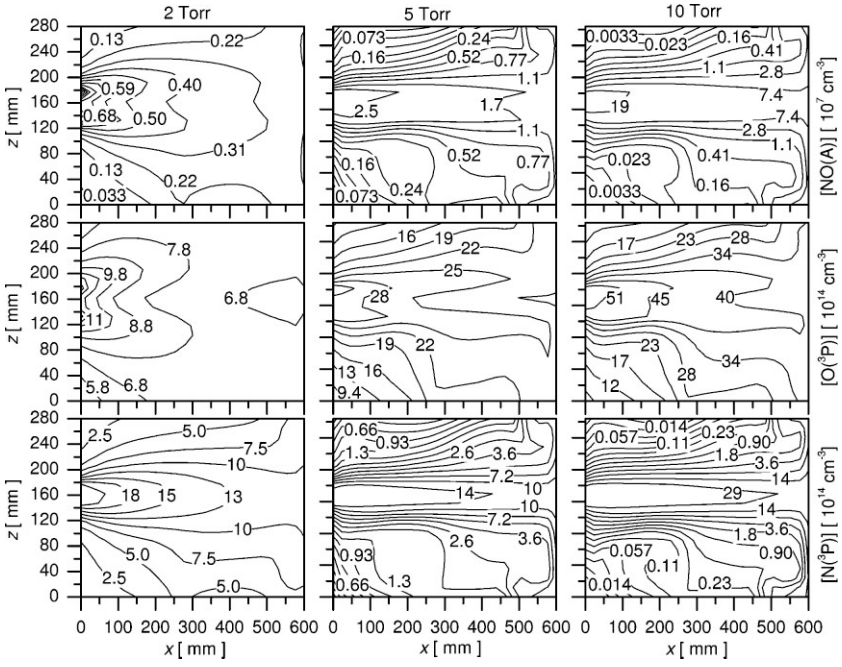

Figure 13. Calculated density distributions in the x–z plane at $y = 150$ mm in the reactor chamber for three gas pressures at a 1 000 sccm N_2 flow rate and 15 sccm of added O_2 (1.5%) at 2 450 MHz. NO(A) (first row), O(^{3}P) (second row) and N(^{4}S) (third row). The densities are given in 10^7 cm^{-3} units for NO(A) and in 10^{14} cm^{-3} units for O(^{3}P) and N(^{4}S).

6 Conclusion

The aim of the present modelling was to account for the observed spatial distribution of the UV emission intensity in a chamber filled with a low-pressure N_2–O_2 flowing afterglow in which sterilization is to be conducted. This has required determining the appropriate set of kinetic reactions occurring in the early and late afterglows that provide the density of the upper state of the UV emission transitions. A close comparison between numerical results and experimental data has enabled us, on the one hand, to retain the essential species involved and thus to neglect contributions from some excited (metastable and vibrational) neutral states and ion species, and, on the other hand, forced us to include a kinetic pathway for the formation of the NO(A) level that had been omitted in all previous publications dealing with

DOI: 10.1002/ppap.200800085

the N_2–O_2 late afterglow, namely $N(^4S) + O(^3P) + (N_2) \rightarrow NO(A) + (N_2)$. The results of this modelling, which fit almost all experimental data (except for the effect of high gas pressure on the absolute density of the NO(A) state), point out to the dominant kinetic processes at the origin of the NO_γ UV emission intensity and governing its spatial distribution in the afterglow chamber.

Acknowledgements: This work has been supported by the *Portuguese Science Foundation FCT* through project POCTI/FAT/44221/2002 co-financed by FEDER, and through the post-doc fellowship of K. K.

Received: May 23, 2008; Revised: August 8, 2008; Accepted: August 13, 2008; DOI: 10.1002/ppap.200800085

Keywords: afterglow plasma processes; density; hydrodynamic modelling; kinetics; microwave discharges; sterilization; UV irradiation

[1] M. Moisan, J. Barbeau, S. Moreau, J. Pelletier, M. Tabrizian, L'H. Yahia, *Int. J. Pharm.* **2001**, *226*, 1.
[2] O. Kylián, H. Rauscher, D. Gilliland, F. Brétagnol, F. Rossi, *J. Phys. D: Appl. Phys.* **2008**, *41*, 095201.
[3] K. Kelly-Wintenberg, T. C. Montie, C. Brickman, J. R. Roth, A. K. Carr, K. Sorge, L. C. Wadsworth, P. P. Y. Tsai, *J. Ind. Microbiol. Biotechnol.* **1998**, *20*, 69.
[4] H. W. Herrmann, I. Henins, J. Park, G. S. Selwyn, *Phys. Plasmas* **1999**, *6*, 2284.
[5] J. R. Roth, D. M. Sherman, R. B. Gadri, F. Karakaya, Z. Chen, T. C. Montie, K. Kelly-Witenberg, *IEEE Trans. Plasma Sci.* **2000**, *28*, 56.
[6] M. Laroussi, *IEEE Trans. Plasma Sci.* **2002**, *30*, 1409.
[7] M. Heise, W. Neff, O. Franken, P. Muranyi, J. Wunderlich, *Plasmas Polym.* **2004**, *9*, 23.
[8] K.-Y. Lee, B. J. Park, D. H. Lee, I.-S. Lee, S. O. Hyun, K.-H. Chung, J.-C. Park, *Surf. Coat. Technol.* **2005**, *193*, 35.
[9] A. M. Pointu, A. Ricard, B. Dodet, E. Odic, J. Larbre, M. Ganciu, *J. Phys. D: Appl. Phys.* **2005**, *38*, 1905.
[10] H. Ohkawa, T. Akitsu, M. Tsuji, H. Kimura, K. Fukushima, *Plasma Processes Polym.* **2005**, *2*, 120.
[11] M. K. Boudam, M. Moisan, B. Saoudi, C. Popovici, N. Gherardi, F. Massines, *J. Phys. D: Appl. Phys.* **2006**, *39*, 3494.
[12] T. Sato, K. Fujioka, R. Ramasamy, T. Urayama, S. Fujii, *IEEE Trans. Ind. Appl.* **2006**, *42*, 399.
[13] Q. S. Yu, C. Huang, F. H. Hsieh, H. Huff, Y. Duan, *Appl. Phys. Lett.* **2006**, *88*, 013903.
[14] G. Fridman, M. Peddinghaus, H. Ayan, A. Fridman, M. Balasubramanian, A. Gutsol, A. Brooks, G. Fridman, *Plasma Chem. Plasma Process.* **2006**, *26*, 425.
[15] K. Lee, K.-h. Paek, W.-T. Ju, Y. Lee, *J. Microbiol.* **2006**, *44*, 269.
[16] B. J. Park, D. H. Lee, J.-C. Park, I. S. Lee, K. Y. Lee, S. O. Hyun, M. S. Chun, K. H. Chung, *Surf. Coat. Technol.* **2007**, *201*, 5738.
[17] N. Puač, Z. L. Petrović, G. Malović, A. Đorđević, S. Živković, Z. Giba, D. Grubišić, *J. Phys. D: Appl. Phys.* **2006**, *39*, 3514.
[18] J. Feichtinger, A. Schulz, M. Walker, U. Schumacher, *Surf. Coat. Technol.* **2003**, *174–175*, 564.
[19] S. Lerouge, M. R. Wertheimer, R. Marchand, M. Tabrizian, L'H. Yahia, *J. Biomed. Mater. Res.* **2000**, *51*, 128.
[20] M. Nagatsu, F. Terashita, H. Nonaka, L. Xu, T. Nagata, Y. Koide, *Appl. Phys. Lett.* **2005**, *86*, 211502.
[21] F. Rossi, O. Kylian, M. Hasiwa, *Plasma Processes Polym.* **2006**, *3*, 431.
[22] N. Hayashi, W. Guan, Sh. Tsutsui, T. Tomari, Y. Hanada, *Jpn. J. Appl. Phys.* **2006**, *45*, 8358.
[23] L. Xu, H. Nonaka, H. Y. Zhou, A. Ogino, T. Nagata, Y. Koide, S. Nanko, I. Kurakawi, M. Nagatsu, *J. Phys. D: Appl. Phys.* **2007**, *40*, 803.
[24] S. Moreau, M. Moisan, M. Tabrizian, J. Barbeau, J. Pelletier, A. Ricard, L'H. Yahia, *J. Appl. Phys.* **2000**, *88*, 1166.
[25] S. Lerouge, A. C. Fozza, M. R. Wertheimer, R. Marchand, L'H. Yahia, *Plasmas Polym.* **2000**, *5*, 31.
[26] A. Ricard, M. Moisan, S. Moreau, *J. Phys. D: Appl. Phys.* **2001**, *34*, 1203.
[27] N. Philip, B. Saoudi, M.-Ch. Crevier, M. Moisan, J. Barbeau, J. Pelletier, *IEEE Trans. Plasma Sci.* **2002**, *30*, 1429.
[28] V. Monna, C. Nguyen, M. Kahil, A. Ricard, N. Sixou, *IEEE Trans. Plasma. Sci.* **2002**, *30*, 1437.
[29] S. Villeger, S. Cousty, A. Ricard, M. Sixou, *J. Phys. D: Appl. Phys.* **2003**, *36*, L60.
[30] M. Laroussi, *Plasma Processes Polym.* **2005**, *2*, 391.
[31] M. K. Boudam, B. Saoudi, M. Moisan, A. Ricard, *J. Phys. D: Appl. Phys.* **2007**, *40*, 1694.
[32] O. Kylian, T. Sasaki, F. Rossi, *Eur. Phys. J. Appl. Phys.* **2006**, *34*, 139.
[33] M. Moisan, J. Barbeau, M.-Ch. Crevier, J. Pelletier, N. Philip, B. Saoudi, *Pure Appl. Chem.* **2002**, *74*, 349.
[34] R. W. B. Pearse, A. G. Gaydon, "*The Identification of Molecular Spectra*", Chapman & Hall, London 1963.
[35] A. Cabaj, R. Sommer, W. Pribil, T. Haider, *Water Sci. Technol.: Water Supply* **2002**, *12*, 175.
[36] N. Munakata, M. Saito, K. Hieda, *Photochem. Photobiol.* **1991**, *54*, 761.
[37] S. Villeger, S. Cousty, A. Ricard, *Plasma Process. Polym.* **2005**, *2*, 709.
[38] S. Cousty, S. Villeger, J. P. Sarette, A. Ricard, M. Sixou, *Eur. Phys. J. Appl. Phys.* **2006**, *34*, 43.
[39] A. Ricard, V. Monna, M. Mozetic, *Surf. Coat. Technol.* **2003**, *174–175*, 905.
[40] A. Ricard, V. Monna, *Plasma Sources Sci. Technol.* **2002**, *11*, 1.
[41] S. Bockel, A. M. Diamy, A. Ricard, *Surf. Coat. Technol.* **1995**, *74–75*, 474.
[42] M. C. Crevier, M. Moisan, L'H. Yahia, B. Saoudi, *Proc. Int. Symp. on Advanced Materials for Biomedical Applications (SAMBA) (Montréal, Québec)* 2002, 365.
[43] C. D. Pintassilgo, J. Loureiro, V. Guerra, *J. Phys. D: Appl. Phys.* **2005**, *38*, 417.
[44] K. Kutasi, C. D. Pintassilgo, P. J. Coelho, J. Loureiro, *J. Phys. D: Appl. Phys.* **2006**, *39*, 3978.
[45] K. Kutasi, J. Loureiro, *J. Phys. D: Appl. Phys.* **2007**, *40*, 5612.
[46] C. D. Pintassilgo, K. Kutasi, J. Loureiro, *Plasma Sources Sci. Technol.* **2007**, *16*, S115.
[47] K. Kutasi, C. D. Pintassilgo, J. Loureiro, P. J. Coelho, *J. Phys. D: Appl. Phys.* **2007**, *40*, 1990.
[48] V. A. Shakhatov, Yu. A. Lebedev, *High Energy Chem.* **2008**, *42*, 170.
[49] V. Guerra, J. Loureiro, *Plasma Sources Sci. Technol.* **1999**, *8*, 110.
[50] S. Wickramanayaka, S. Meikle, T. Kobayashi, N. Hosokawa, Y. Hanataka, *J. Vac. Sci. Technol. A* **1991**, *9*, 2999.

[51] S. Wickramanayaka, N. Hosokawa, Y. Hanataka, *Jpn. J. Appl. Phys.* **1991**, *30*, 2897.
[52] J. P. Sarrette, B. Rouffet, A. Ricard, *Plasma Processes. Polym.* **2005**, *3*, 120.
[53] M. Moisan, J. Pelletier, Eds., *"Microwave Excited Plasmas"*, Elsevier, Amsterdam 1992.
[54] M. Moisan, Z. Zakrzewski, *J. Phys. D: Appl. Phys.* **1991**, *24*, 1025.
[55] M. Mérel, M. Tabbal, M. Chaker, M. Moisan, A. Ricard, *Plasma Sources Sci. Technol.* **1998**, *7*, 550.
[56] R. W. Gross, N. Cohen, *J. Chem. Phys.* **1968**, *48*, 2582.
[57] F. R. Gilmore, *J. Quant. Spectrosc. Radiat. Transf.* **1965**, *5*, 369.

DOI: 10.1002/ppap.200800085